

## RESEARCH ARTICLE

## CERAMICS

## Plastic deformation in silicon nitride ceramics via bond switching at coherent interfaces

Jie Zhang<sup>1†</sup>, Guanghua Liu<sup>1†</sup>, Wei Cui<sup>1†</sup>, Yiyao Ge<sup>1</sup>, Songmo Du<sup>1</sup>, Yixuan Gao<sup>2</sup>, Yuyang Zhang<sup>2</sup>, Fei Li<sup>1</sup>, Zhanglin Chen<sup>1</sup>, Shixuan Du<sup>2</sup>, Kexin Chen<sup>3\*</sup>

Covalently bonded ceramics exhibit preeminent properties—including hardness, strength, chemical inertness, and resistance against heat and corrosion—yet their wider application is challenging because of their room-temperature brittleness. In contrast to the atoms in metals that can slide along slip planes to accommodate strains, the atoms in covalently bonded ceramics require bond breaking because of the strong and directional characteristics of covalent bonds. This eventually leads to catastrophic failure on loading. We present an approach for designing deformable covalently bonded silicon nitride ( $\text{Si}_3\text{N}_4$ ) ceramics that feature a dual-phase structure with coherent interfaces. Successive bond switching is realized at the coherent interfaces, which facilitates a stress-induced phase transformation and, eventually, generates plastic deformability.

Covalently bonded ceramics such as silicon nitride ( $\text{Si}_3\text{N}_4$ ) have attractive mechanical, chemical, and physical properties that feature high-temperature tolerance, superior hardness, excellent wear and corrosion resistance, relatively high thermal conductivity, and electrical insulation. These

properties make the ceramics suitable for applications such as high-temperature structural materials, cutting tools, bearings, and substrates in electronic packaging (1–5). For example, metal components in gas turbine engines are replaced with covalently bonded ceramics to improve efficiency (6–8). However, ceramics

tend to be brittle, such that even a tiny crack can lead to catastrophic failures without observable plastic deformation. This problem severely restricts the applicability of ceramics. Mechanistically, because of the strong and directional characteristic of covalent bonds, local plastic deformation in covalently bonded ceramics is normally initiated via the bond-breaking mechanism (9). Unfortunately, this process induces nucleation, growth, and coalescence of nanopores, eventually leading to brittle fracture (10). Although numerous efforts have been devoted to toughening covalently bonded ceramics by interlocking the microstructures with elongated grains or designing laminated structures (11–21), and certain deformability of amorphous ceramics has been observed (22–24), covalently bonded crystalline deformable ceramics have yet to be achieved as a result of the intrinsic strong and directional characteristics of covalent bonds. As such,

<sup>1</sup>State Key Laboratory of New Ceramics and Fine Processing, School of Materials Science and Engineering, Tsinghua University, Beijing 100084, P.R. China. <sup>2</sup>University of Chinese Academy of Sciences, Chinese Academy of Sciences, Beijing 100190, P.R. China. <sup>3</sup>Department of Engineering and Material Sciences, National Natural Science Foundation of China (NSFC), Beijing 100085, P.R. China.

\*Corresponding author. Email: kxchen@mails.tsinghua.edu.cn  
†These authors contributed equally to this work.

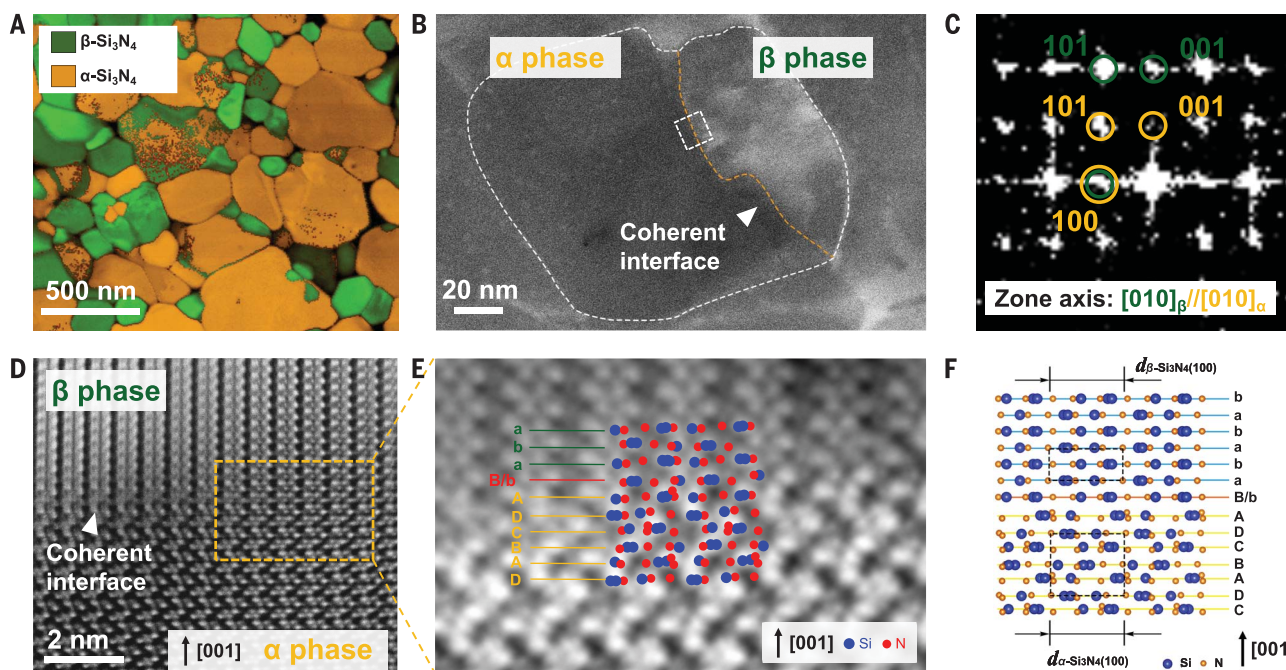


**Fig. 1. Microstructure of dual-phase  $\alpha/\beta\text{-Si}_3\text{N}_4$  ceramics with coherent interfaces.** (A) Phase map of the  $\alpha/\beta\text{-Si}_3\text{N}_4$  sample with precession electron diffraction. (B) TEM image of an  $\alpha/\beta$  coherent interface (highlighted by the orange dashed line). The white dashed line indicates the outline of the  $\text{Si}_3\text{N}_4$  grain. The area enclosed by the white dashed square is discussed in (D). (C) Fast Fourier transform at the interface shows that the  $\alpha$  and  $\beta$  subgrains have a specific orientation relationship of  $[010]_\alpha//[010]_\beta$ ,  $[001]_\alpha//[001]_\beta$ , and  $(100)_\alpha//(100)_\beta$ . (D) HAADF-STEM image showing the  $\alpha$  and  $\beta$  phase atomically

matched along the  $[001]$  direction at the interface. The image corresponds to the area marked by the white dashed square in (B) and is rotated here to make the coherent interface horizontal. (E) Close-up iDPC-STEM image [corresponding to the area marked by the orange dashed square in (D)] showing the atomic stacking order at the coherent interface; the B-layer atoms of the  $\alpha$  phase are shared with the  $\beta$  phase to form the interface atomic layer. (F) Atomic model corresponding to the observation; Si and N atoms are represented as blue and orange spheres, respectively.  $d$ ,  $d$ -spacing in the crystal.

realizing the plastic deformability of covalently bonded crystalline ceramics has been a long-standing and critical challenge.

Macroscopic plastic deformation in response to external loading is often an accumulative result of successive multiple atomic displacements. In alloys with metallic bonds, plastic deformation is realized by local atomic displacements that proceed through switching one or a few interatomic bonds at a time along the lattice planes, also known as dislocation motion (25, 26). Stress-induced phase transformation and the consequent plasticity have been realized in metallic materials and even in ionically bonded ceramics such as  $\text{ZrO}_2$  (27–32) with nondirectional bonding. Although this mechanism has enabled plastic deformation in other materials, it has remained elusive in covalently bonded ceramics (33), mainly because of the directionality of covalent bonds.

Theoretically, it could be possible to achieve macroscopic plastic deformation in covalently bonded ceramics provided that bond breaking in covalent bonds occurs in a very small volume together with immediate healing by new bond formations, which we define as bond switching in this text. In this sense, the energy barrier needs to be lower for local atomic rearrangement to enable a relatively easy transition of one bonding configuration to another, and simultaneously, the lattices on both sides of the slip plane must have roughly the same unit atomic distance to ensure successive atomic translation in crystalline ceramics (34).

Accordingly, a dual-phase structure with a coherent interface may meet these requirements and serve as a good candidate to realize phase transformation-mediated plastic deformation via bond switching in covalently bonded crystalline ceramics. Here, we demonstrate this design strategy in  $\text{Si}_3\text{N}_4$ , a typical covalently bonded crystalline ceramic of wide interest (35–40). Under normal conditions,  $\text{Si}_3\text{N}_4$  has two polymorphs, the  $\alpha$  and  $\beta$  phases. These two polymorphs have similar hexagonal lattice structures composed of corner-shared  $[\text{SiN}_4]$  tetrahedra, that is, their lattice constant is almost the same along the  $a$  direction but differs along the  $c$  direction, with the lattice constant of  $\alpha$  being twice that of  $\beta$  (41, 42). Such a crystallographic configuration allows  $\text{Si}_3\text{N}_4$  to potentially possess coherent phase interfaces in the crystals. Given this, we designed a dual-phase  $\alpha/\beta\text{-Si}_3\text{N}_4$  ceramic with coherent interfaces and observed substantial plastic deformation in the ceramic.

#### Microstructure characterization of $\alpha/\beta\text{-Si}_3\text{N}_4$ with coherent interfaces

Bulk  $\text{Si}_3\text{N}_4$  ceramics are usually prepared by liquid-phase sintering from  $\alpha\text{-Si}_3\text{N}_4$  powder, in which the  $\alpha \rightarrow \beta$  phase transformation occurs

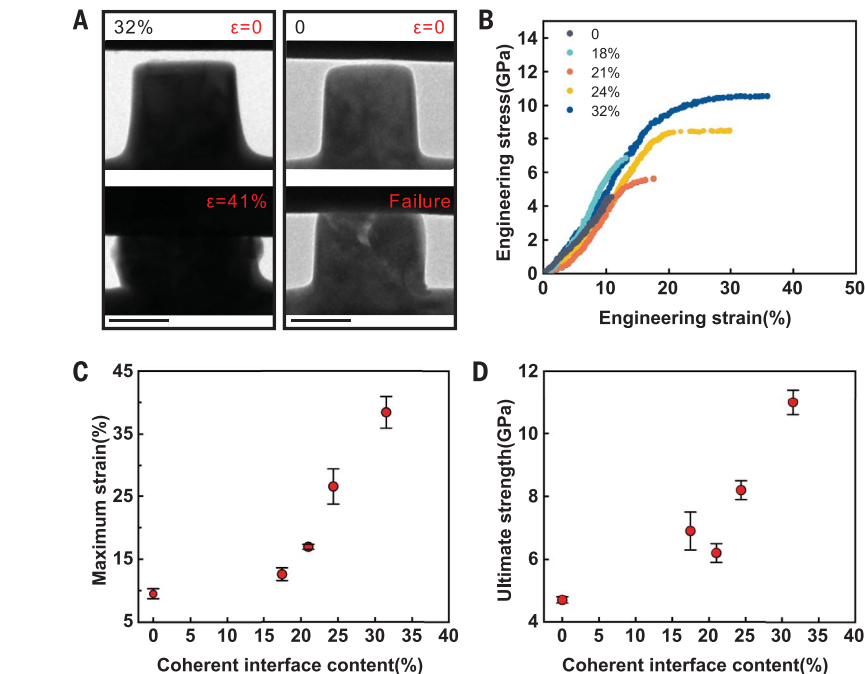


**Fig. 2. Mechanical behaviors of polycrystalline  $\text{Si}_3\text{N}_4$  nanopillars with different proportions of coherent interfaces (proportion of the total length of the interfaces).** (A) A series of TEM images of  $\alpha/\beta\text{-Si}_3\text{N}_4$  (coherent interface content is 32%) and  $\beta\text{-Si}_3\text{N}_4$  (coherent interface content is 0) nanopillars recorded during the in situ test; the coherent interface content was tested by transmission Kikuchi diffraction (fig. S4). The scale bars are 200 nm, and both the nanopillars have a diameter of about 350 nm.  $\epsilon$ , compression strain. (B) Nanopillars with a richer coherent interface showing higher engineering stress-strain. (C and D) The measured maximum strain (C) and ultimate strength (D) versus coherent interface content showing that both the maximum strain and ultimate strength simultaneously increase with the proportion of coherent interface ( $N = 5$ , where  $N$  is the number of samples used to calculate the average value and the error of each data point). Error bars represent SD.

via the dissolution-precipitation mechanism (43, 44), and consequently, the sintered dense  $\text{Si}_3\text{N}_4$  ceramics are mostly single-phase  $\beta\text{-Si}_3\text{N}_4$ . Using a method that largely differs from the conventional process, we prepared the dual-phase  $\alpha/\beta\text{-Si}_3\text{N}_4$  ceramics (hereafter referred to as  $\alpha/\beta\text{-Si}_3\text{N}_4$ ) with a varying fraction of coherent  $\alpha/\beta$  phase interfaces through precise control of the sintering parameters to quench the  $\alpha \rightarrow \beta$  transformation (45). During this process, the  $\alpha$ - and  $\beta\text{-Si}_3\text{N}_4$  grains with a specific orientation relationship were directly integrated (Fig. 1).

We examined the microstructure of  $\alpha/\beta\text{-Si}_3\text{N}_4$  using high-angle annular dark-field scanning transmission electron microscopy (HAADF-STEM). The sample showed a dual-phase grain structure, where each grain consists of both  $\alpha$ - and  $\beta\text{-Si}_3\text{N}_4$  with a coherent interface between the two phases (Fig. 1, A and B). Further analysis at the interfaces shows that the  $\alpha$  and  $\beta$  subgrains have a specific orientation relationship of  $[001]_{\alpha} // [001]_{\beta}$  and  $(100)_{\alpha} // (100)_{\beta}$  (Fig. 1C and fig. S1), where the angle mismatch between the  $\alpha$  and  $\beta$  subgrains is less than  $1.8^\circ$  (Fig. S2). We did not observe sharp interfaces, indicating a high degree of lattice matching

between the  $\alpha$ - and  $\beta\text{-Si}_3\text{N}_4$  (Fig. 1D). The integrated differential phase contrast (iDPC)-STEM image of the interface (Fig. 1E) along the  $[010]$  direction shows the atomic columns with periodically strong and weak intensities, corresponding to the atomic stacking sequence of  $\cdots\text{ABCDBABabab}\cdots$  along the  $[001]$  direction. Based on the iDPC-STEM images, we established a structure model (Fig. 1F) to schematically reveal the highly coherent interface at the atomic scale. To achieve atomic-scale matching in  $\alpha/\beta\text{-Si}_3\text{N}_4$ , a small lattice distortion caused by a slight difference in the interplanar spacings of  $(100)$  planes of the  $\alpha$  and  $\beta$  phases still exists in the  $\beta$  grain, which agrees with the result of strain field analysis (fig. S3). Clearly, the coherent  $\alpha/\beta$  interface is largely distinguished from the conventional grain interfaces in  $\text{Si}_3\text{N}_4$  ceramics, where two randomly oriented grains are separated by an intergranular glassy film (38, 39).

#### Mechanical properties of $\alpha/\beta\text{-Si}_3\text{N}_4$ by nanopillar compression

We evaluated the mechanical properties of the  $\alpha/\beta\text{-Si}_3\text{N}_4$  samples by nanopillar compression

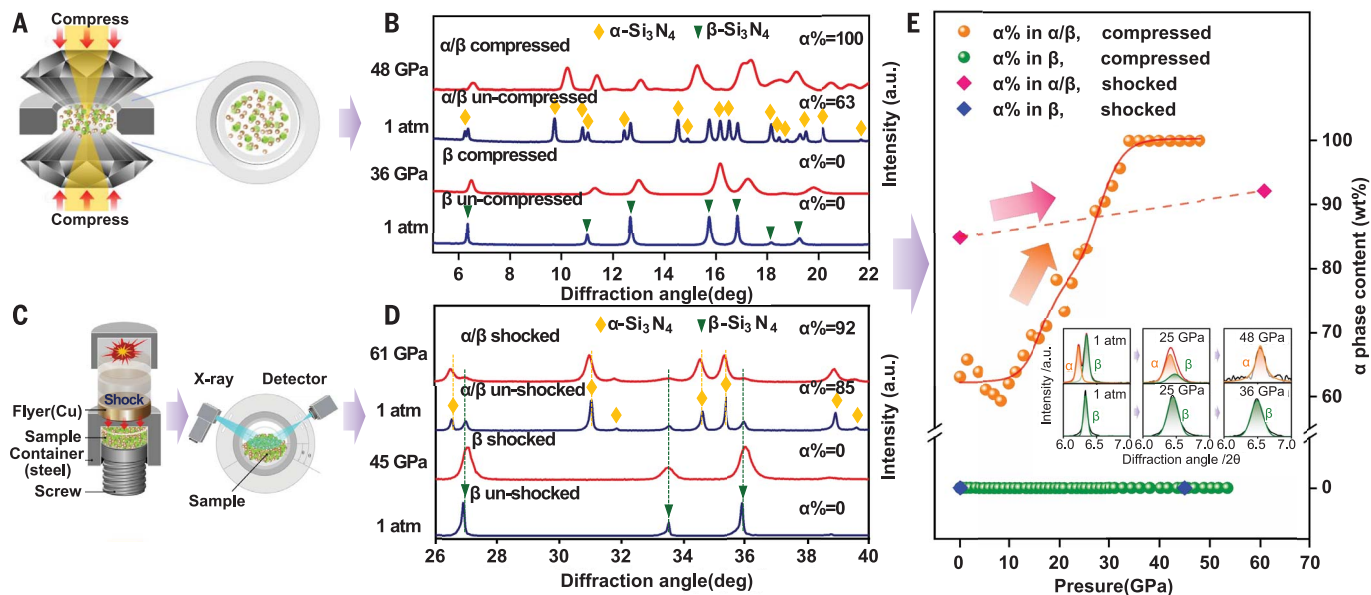


**Fig. 3. Phase-content change of  $\text{Si}_3\text{N}_4$  samples during compression under high pressure.** (A) Schematic diagram of the ADXRD test under uniaxial pressure; the wavelength of the monochromatic x-ray beam was 0.7293 Å. (B) Selected x-ray diffraction (XRD) spectra of  $\beta\text{-Si}_3\text{N}_4$  and  $\alpha/\beta\text{-Si}_3\text{N}_4$ . The diffraction peak shifted to the right for pure  $\beta\text{-Si}_3\text{N}_4$ , the  $\alpha$  phase never appeared, and the  $\beta$  phase remained stable up to 36 GPa; by contrast, the  $\beta$  phase gradually decreased until it could not be detected up to 48 GPa in  $\alpha/\beta\text{-Si}_3\text{N}_4$ . a.u., arbitrary units. (C) Schematic diagram of the shock experiment; the sample was shocked through high-speed flyer (Cu) and then the phase content was detected by XRD. The monochromatic x-ray beam had a wavelength of 1.54178 Å. (D) XRD spectra of  $\beta\text{-Si}_3\text{N}_4$  and  $\alpha/\beta\text{-Si}_3\text{N}_4$  before and after shocking. The  $\beta$  phase remained stable after shocking by  $\sim 45$  GPa in pure  $\beta\text{-Si}_3\text{N}_4$ , and no  $\alpha$  phase was observed even though obvious lattice

distortion of the  $\beta$  phase was induced, as indicated by the peak shift. By contrast, the diffraction intensity of the  $\beta$  phase decreased in  $\alpha/\beta\text{-Si}_3\text{N}_4$  after shocking; thus, the content of the  $\alpha$  phase increased by  $\sim 7\%$ . (E) Variation in the  $\alpha$  phase content under pressure. The  $\alpha$  phase content in  $\alpha/\beta\text{-Si}_3\text{N}_4$  gradually increased as the pressure increased; under static pressure, the  $\beta$  phase gradually transformed to the  $\alpha$  phase and almost completely transformed at  $\sim 34$  GPa in  $\alpha/\beta\text{-Si}_3\text{N}_4$ . Under shock load, the  $\beta \rightarrow \alpha$  transformation could still occur, but the amount of phase transformation was less than that under static pressure because the duration of the peak pressure was extremely short. In pure  $\beta\text{-Si}_3\text{N}_4$ , the  $\beta \rightarrow \alpha$  transformation could not happen, irrespective of the type of stress stimulus. The insets show the (110) diffraction peaks of the  $\alpha$  and  $\beta$  phases in  $\alpha/\beta\text{-Si}_3\text{N}_4$  (top) and  $\beta\text{-Si}_3\text{N}_4$  (bottom) after compression under different pressures.

tests. During the sintering of  $\text{Si}_3\text{N}_4$  ceramics, densification usually occurs along with the  $\alpha \rightarrow \beta$  phase transformation; both densification and phase transformation are thermally activated and achieved by the dissolution-precipitation mechanism (43, 44). To prepare our  $\alpha/\beta\text{-Si}_3\text{N}_4$  samples containing coherent  $\alpha/\beta$  interfaces, both lowering the sintering temperature and shortening the holding time are required to limit the  $\alpha \rightarrow \beta$  phase transformation and hamper the densification process. As a result, the prepared  $\alpha/\beta\text{-Si}_3\text{N}_4$  samples are not fully dense and are prone to contain defects such as pores. The mechanical properties of covalently bonded ceramics are sensitive to these defects, which affect crack generation and propagation and, consequently, may cause a deterioration of mechanical behavior (9). To minimize the ambiguities caused by the structural defects and reveal the intrinsic properties of the prepared  $\alpha/\beta\text{-Si}_3\text{N}_4$  samples, we therefore used nanopillar-shaped samples (rectangular nanopillars of about 350 nm by 350 nm by 250 nm) to evaluate the mechanical properties (45).

The  $\alpha/\beta\text{-Si}_3\text{N}_4$  nanopillars exhibited higher strength and plastic deformation compared with conventional  $\beta\text{-Si}_3\text{N}_4$  fractured just in the elastic deformation stage (Fig. 2, A and B, and figs. S5 to S9). The  $\alpha/\beta\text{-Si}_3\text{N}_4$  nanopillar (coherent interface proportion of  $\sim 32\%$ ) showed a fracture strength of  $11.0 \pm 0.4$  GPa and a plastic strain of about 20% (Fig. 2, C and D, and movie S1). For comparison, a conventional  $\beta\text{-Si}_3\text{N}_4$  nanopillar of almost the same size showed a fracture strength of  $4.7 \pm 0.1$  GPa with no plastic deformation (Fig. 2, C and D, and movie S2). The plastic deformation of  $\alpha/\beta\text{-Si}_3\text{N}_4$  under uniaxial compression is quite different from the localized deformation under confined compression that is observed in nano-indentation tests (46). The  $\text{Si}_3\text{N}_4$  nanopillars exhibited an elastic strain of  $\sim 10\%$ , which is considerably larger than those observed in bulk  $\text{Si}_3\text{N}_4$  samples mainly because of the small sample size. Similar results have been reported for other ceramics; for instance, an elastic strain of  $\sim 8\%$  was observed during the compression of  $\text{MgAl}_2\text{O}_4$  micropillars with

a diameter of 2.5  $\mu\text{m}$  at room temperature, which is much larger than that of the bulk samples ( $<1\%$ ) (47). Furthermore, the strength and plasticity of the  $\alpha/\beta\text{-Si}_3\text{N}_4$  samples showed a strong dependence on the proportion of  $\alpha/\beta$  coherent interfaces in all the interfaces. By increasing the proportion of coherent interfaces, we simultaneously enhanced the plasticity and strength considerably (Fig. 2, C and D). The effect of electron beam irradiation on the plasticity of the  $\alpha/\beta\text{-Si}_3\text{N}_4$  nanopillars was negligible, which we confirmed by nanopillar compression tests with the electron beam switched off (fig. S10).

#### Stress-induced $\beta \rightarrow \alpha$ phase transformation in $\alpha/\beta\text{-Si}_3\text{N}_4$

To investigate the structural evolution upon external loading, we performed in situ static compression under angle dispersive x-ray diffraction (ADXRD) on the  $\alpha/\beta\text{-Si}_3\text{N}_4$  and  $\beta\text{-Si}_3\text{N}_4$  samples (Fig. 3A). The  $\beta \rightarrow \alpha$  phase transformation began at a pressure of  $\sim 10$  GPa and completed at  $\sim 35$  GPa during the compression

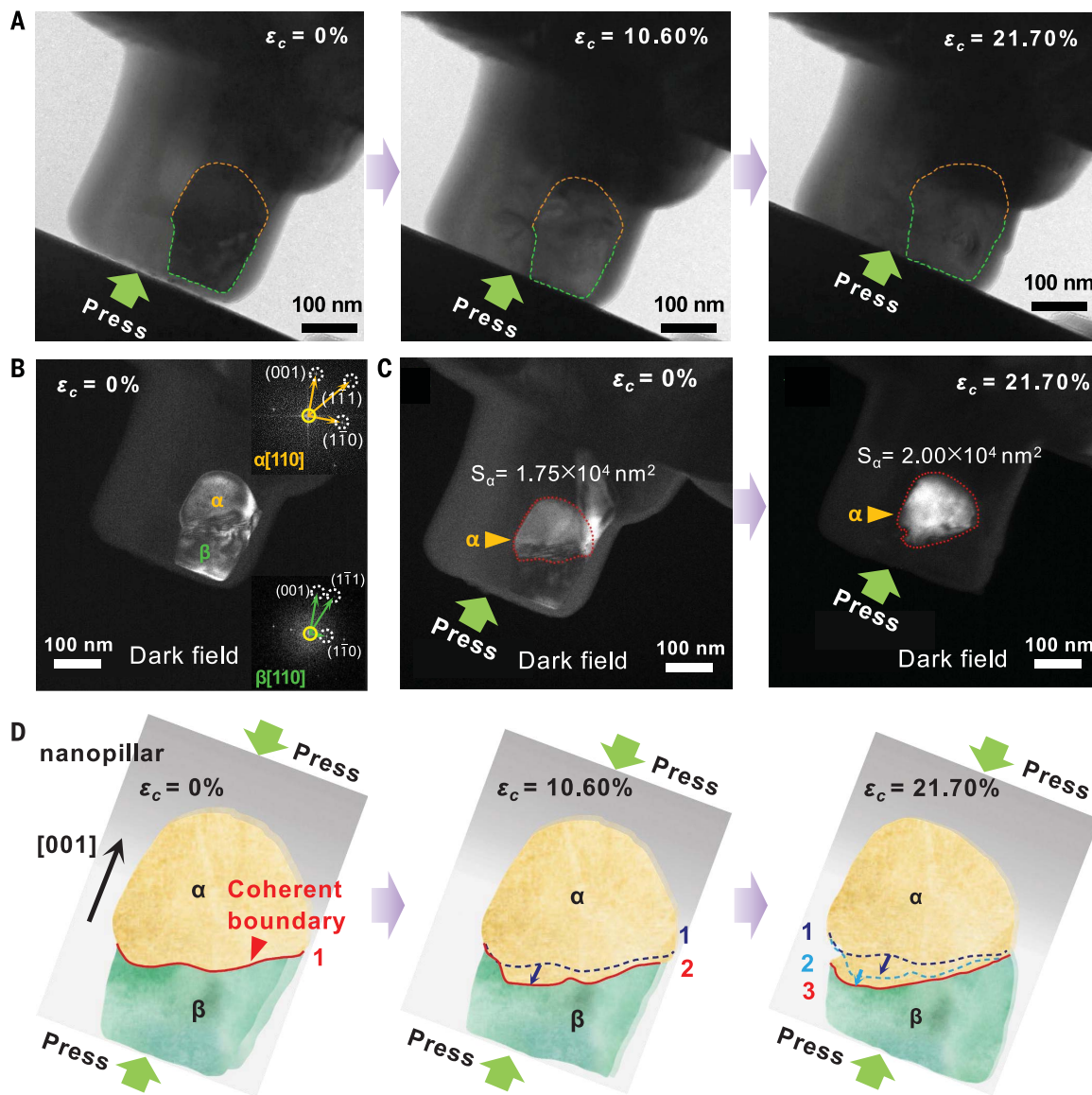


**Fig. 4. A representative  $\beta \rightarrow \alpha$  phase transformation event revealed by in situ TEM.** (A) Bright-field images of a nanopillar at different compression strains ( $\epsilon_c = 0, 10.60,$  and  $21.70\%$ ); the orange and green dashed lines show the outlines of the  $\alpha$  and  $\beta$  grains, respectively, with coherent interfaces; outside of the dashed lines in the nanopillar are the  $\text{Si}_3\text{N}_4$  grains bonded by the glass phase. The nanopillar was compressed by the diamond flat indenter shown in the bottom-left corner of the image. (B) Coherent structure caused the diffraction patterns of  $(1-10)_\alpha$  and  $(1-10)_\beta$  to overlap; hence, the dark-field image [diffraction beam of  $(1-10)$  was captured] reveals the outlines of the  $\alpha$  and  $\beta$  grains. (C) When the diffraction beam of the  $(001)_\alpha$  was captured,

only the  $\alpha$  grain appeared bright in the dark-field image; the projected area of the  $\alpha$  grain along the electron beam ( $S_\alpha$ ) is  $\sim 1.75 \times 10^4 \text{ nm}^2$ , and the bottom of the  $\alpha$  grain is the coherent interface with the  $\beta$  grain. After compression, the coherent interface extended into the  $\beta$  grain, and  $S_\alpha$  increased to  $\sim 2.00 \times 10^4 \text{ nm}^2$ . The image drift during in situ compression was negligible, which was confirmed by comparing the contours of the grains in dark-field images before and after compression. (D) Sketch maps of this nanopillar at three compression stages show the movement of the coherent interface more clearly during the compression process. The coherent interface that separates the grains is denoted by the red line and is labeled 1, 2, and 3.

of the  $\alpha/\beta\text{-Si}_3\text{N}_4$  sample (Fig. 3, B and E, and fig. S11). The onset pressure for the  $\beta \rightarrow \alpha$  phase transformation here is higher than the yield stress of  $\alpha/\beta\text{-Si}_3\text{N}_4$  nanopillars that we observed in the uniaxial compression tests (Fig. 2B), mostly because the sample here is compressed under a constrained condition (48). After unloading to 0.1 MPa, only the  $\alpha$  phase existed and no  $\beta$  phase was detected (fig. S12). During

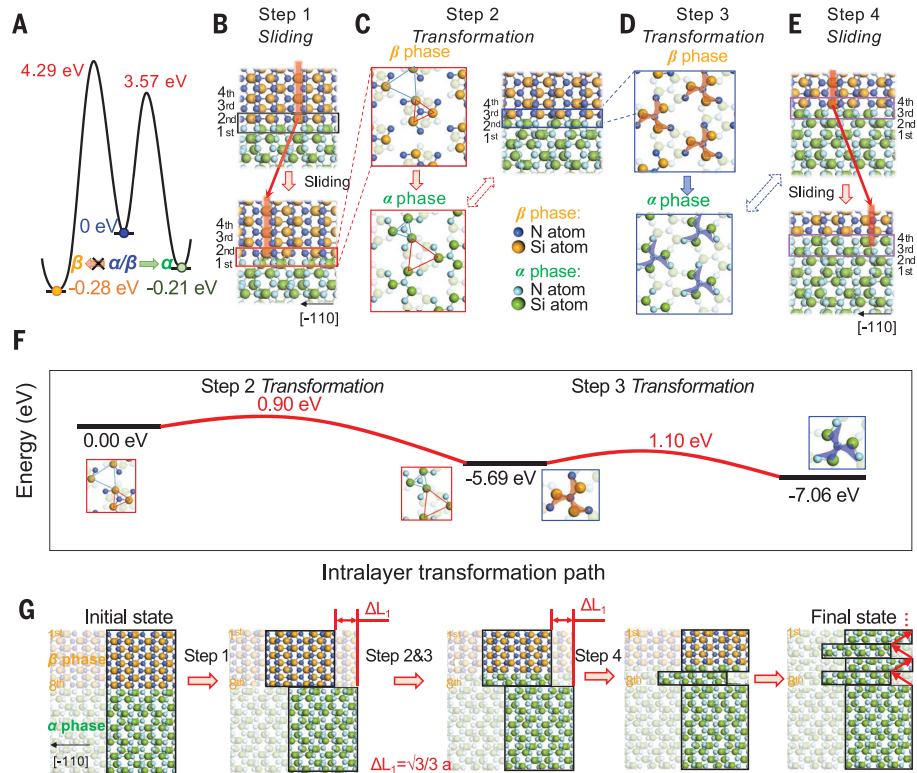
the compression of the single-phase  $\beta\text{-Si}_3\text{N}_4$  sample, however, we did not observe any  $\beta \rightarrow \alpha$  phase transformation, even under the maximum pressure of 54 GPa (Fig. 3B and fig. S13) and unloading to 0.1 MPa (fig. S14). Furthermore, we performed dynamic compression experiments for the  $\alpha/\beta\text{-Si}_3\text{N}_4$  and  $\beta\text{-Si}_3\text{N}_4$  samples (Fig. 3C). We used explosion shock to generate a pulse of pressure on the sample

with a peak stress of  $\sim 61$  GPa. We observed the  $\beta \rightarrow \alpha$  phase transformation during compression of the  $\alpha/\beta\text{-Si}_3\text{N}_4$  sample (which was incomplete due to the extremely short time duration of high pressure) (Fig. 3D). The transformation was absent in the conventional  $\beta\text{-Si}_3\text{N}_4$  sample.

The structural evolution that we observed during both static and dynamic compression

### Fig. 5. Density functional theory calculations showing the pathway of the $\beta \rightarrow \alpha$ phase transformation.

(A) Energy landscape of  $\alpha$ ,  $\beta$ , and  $\alpha/\beta$  dual-phase with coherent interface. The energy barrier for the transformation of the  $\alpha/\beta$  dual-phase structure to  $\alpha$  is much lower than that of the transformation to  $\beta$ . (B) Side view of an  $\beta(001)/\alpha(001)$  interface before (top) and after (bottom) sliding along the  $[-110]$  direction by  $\frac{\sqrt{3}}{3}a$ , in which  $a$  is the lattice constant of the supercell. In step 1, the  $\beta$  phase slides along the  $[-110]$  direction with respect to the  $\alpha$  phase. The orange vertical lines and the red arrow are used to highlight the sliding direction. (C) Shown are the top views of the first and second layers in the bottom panel of (B) (top left) and the final state after the second layer transforms to the  $\beta$  phase (bottom left). The side view of the supercell after the phase transformation is shown at the top right. In step 2, the second layer of the  $\beta$  phase transformed to the  $\alpha$  phase after the breaking and rebonding of the Si-N bonds. (D) The top view of the second and third layers in the top right panel of (C) (top) and the final state after the third layer transformed to the  $\beta$  phase (bottom). In step 3, the Si atoms in the third layer of the  $\beta$  phase rotate around the central N atoms, as indicated by the windmills, resulting in the third layer of the  $\beta$  phase transforming to the  $\alpha$  phase. (E) The side views of the structure in the bottom panel of (D) (top) and the structure after sliding (bottom). In step 4, after the whole  $\beta$  phase slides along the  $[-110]$  direction by  $\frac{\sqrt{3}}{3}a$ , the stacking sequence of the fourth layer of the  $\beta$  phase changes to the  $\alpha$  phase naturally. (F) Density functional theory-calculated energy profile of the interface transformation steps shown in (C) and (D). (G) The shearing of original  $\beta$  atom layers with respect to the  $\alpha$  phase during the  $\beta \rightarrow \alpha$  phase transformation. Atoms in the same supercell are highlighted to track the corresponding atoms in each step. The orange and blue spheres represent Si and N atoms in the  $\beta$  phase, whereas the green and light blue spheres represent those in the  $\alpha$  phase, respectively.



confirmed the occurrence of a stress-induced  $\beta \rightarrow \alpha$  phase transformation in  $\text{Si}_3\text{N}_4$ . In the past few decades, only the  $\alpha \rightarrow \beta$  phase transformation was recognized to take place, whereas the  $\beta \rightarrow \alpha$  transformation has been strictly limited because of the higher stability of  $\beta$  compared with  $\alpha$ . The  $\beta \rightarrow \alpha$  phase transformation has not been observed at any temperature and pressure (including at tens of GPa) (49–51). The  $\beta \rightarrow \alpha$  transformation that we observed is intrinsically different from the well-known  $\alpha \rightarrow \beta$  transformation, which is a thermally induced dissolution-precipitation process with the presence of a liquid phase and strongly relies on its diffusion property. It appears that the  $\beta \rightarrow \alpha$  transformation is a stress-induced, diffusionless solid-state phase transformation with no liquid participation. We also found that the stress-induced  $\beta \rightarrow \alpha$  phase transformation only occurred in the  $\alpha/\beta\text{-Si}_3\text{N}_4$  sample but not in the  $\beta\text{-Si}_3\text{N}_4$  sample, indicating a close relation to the dual-phase structure, especially with the coherent interface of our  $\alpha/\beta\text{-Si}_3\text{N}_4$  sample.

We used in situ transmission electron microscopy (TEM) to reveal the role of the coherent  $\alpha/\beta$  interface during the stress-induced  $\beta \rightarrow \alpha$

phase transformation. We compressed an  $\alpha/\beta\text{-Si}_3\text{N}_4$  nanopillar approximately along the  $[001]$  direction of the highlighted grains of the  $\alpha$  and  $\beta$  phases with a coherent interface (Fig. 4A) and monitored the movement of the coherent  $\alpha/\beta$  interface in a dual-phase grain. In the nanopillar, the orange and green dashed lines in Fig. 4A indicate the boundaries of the  $\alpha$  and  $\beta$  subgrains, respectively, with the same orientation in the dark-field image (Fig. 4B). During compression (movie S3), the coherent  $\alpha/\beta$  interface moved to the  $\beta$  subgrain and the  $[001]$ -projected area of the  $\alpha$  subgrain ( $S_\alpha$ ) increased from  $1.75 \times 10^4$  to  $2.00 \times 10^4$   $\text{nm}^2$  (Fig. 4C). Figure 4D illustrates that the stress-induced  $\beta \rightarrow \alpha$  phase transformation is related to the movement of the coherent interface during compression.

#### Mechanism of the $\beta \rightarrow \alpha$ phase transformation in $\alpha/\beta\text{-Si}_3\text{N}_4$

We simulated the detailed atomic movement on the coherent interface using first-principle calculations based on a supercell with a coherent  $\alpha/\beta$  interface. The supercell contains 8 atomic layers of the  $\beta$  phase and 12 atomic layers of the  $\alpha$  phase, as shown in the top panel

of Fig. 5B and fig. S16. The transformation energy barrier from  $\alpha/\beta\text{-Si}_3\text{N}_4$  to  $\beta$  phase is higher than that from  $\alpha/\beta\text{-Si}_3\text{N}_4$  to  $\alpha$  phase (Fig. 5A), which makes the transformation to  $\alpha$  phase more energetically favorable. By comparing all possible pathways of the  $\beta \rightarrow \alpha$  phase transformation (see figs. S15 and S16), we rationalized the following pathway for the  $\beta \rightarrow \alpha$  phase transformation. The pathway contains four steps: The first step involves sliding at the  $\beta/\alpha$  interface, followed by two steps of intralayer transformation, and a final step of sliding at the newly formed  $\beta/\alpha$  interface (Fig. 5, B to E). In the first step, an energy minimum occurs at a displacement of  $\frac{\sqrt{3}}{3}a$  (where  $a$  is the lattice constant of the supercell) when the  $\beta$  phase layers slide along the  $[-110]$  direction (Fig. 5C and fig. S15A). In the second step (Fig. 5C), the second layer (marked in Fig. 5B), which belongs to the  $\beta$  phase, transforms to the  $\alpha$  phase via a bond breaking and rebonding process (marked by the blue and red triangles in Fig. 5C) with an energy barrier of 0.90 eV (Fig. 5F). The bond breaking and rebonding process is also observed in our ab initio molecular dynamics simulations (fig. S17 and movie S4). In the third step, the Si atoms in the

third layer rotate around the central N atoms, leading to the transformation from  $\beta$  phase to  $\alpha$  phase (highlighted by orange and blue windmills in Fig. 5D) with an energy barrier of 1.10 eV. In the final step (purple rectangles in Fig. 5E), the  $\beta$  phase layers slide along the [1-10] direction by  $\frac{\sqrt{3}}{3}a$ , resulting in a stacking layer of  $\alpha$  phase (see fig. S15B for the energy profile). Therefore, the three neighboring layers in the  $\beta$  phase are all transformed to the  $\alpha$  phase during this process. Because the atomic structure of the first layer in the  $\alpha$  phase is the same as that of the fifth layer in the  $\beta$  phase and the periodicity in the  $\alpha$  phase along the [001] direction is four layers, the remaining  $\beta$  phase could eventually transform to the  $\alpha$  phase by continuing this process.

The pathways are characteristic of bond switching of Si-N bonds, [NSi<sub>3</sub>] unit rotation, and structure distortion at the interface (figs. S17 to S21 and movie S4). One crucial process is the sliding along the [-110] direction, which is involved in both the first and fourth steps (figs. S18 and S21) and leads to a shearing between the two subgrains. Bond breaking and rebonding of Si atoms with N (or Si) atoms participate in the process, where the rebonding between the Si atom and another N atom occurs immediately after the preceding Si-N breaking, resulting in bond switching. Such a bond switching mechanism fundamentally differs from the conventional bond-breaking mechanism that leads to crack formation.

As elaborated on earlier, the coherent interfaces between  $\alpha$ - and  $\beta$ -Si<sub>3</sub>N<sub>4</sub> facilitate the rebonding of atoms after bond breaking, giving rise to a bond-switching process without initiating a crack, which always occurs in a conventional bond breaking process. The atomic-scale sliding leads to a displacement between the  $\alpha$  and  $\beta$  subgrains and subsequently the [NSi<sub>3</sub>] unit rotation, as well as structure distortion, at the interface (Fig. 5G and figs. S17 to S21). The accumulation of successive atomic reshufflings from bond switching results in the stress-induced  $\beta \rightarrow \alpha$  phase transformation and the subsequent macroscopic deformability. However, the  $\beta \rightarrow \alpha$  phase transformation dissipates energy to release the strain, which helps to avoid fracturing failure and thus increase the strength. Consequently, the internal stress in the  $\alpha/\beta$ -Si<sub>3</sub>N<sub>4</sub> sample was lower than that in the single-phase  $\beta$ -Si<sub>3</sub>N<sub>4</sub> after dynamic compression (fig. S22 and table S1).

The stress-induced  $\beta \rightarrow \alpha$  phase transformation of Si<sub>3</sub>N<sub>4</sub> is different from the martensitic t $\rightarrow$ m phase transformation of ZrO<sub>2</sub>, despite their similarities of being diffusionless and leading to plastic deformation. ZrO<sub>2</sub> is composed of ionic bonds, in which the t $\rightarrow$ m phase transformation is displacive and realized by a lattice shearing. By contrast, Si<sub>3</sub>N<sub>4</sub> consists of directional covalent bonds, and the  $\beta \rightarrow \alpha$

transformation cannot be achieved by a lattice shearing but instead involves an extra rotation of [NSi<sub>3</sub>] units, which makes the  $\beta \rightarrow \alpha$  phase transformation reconstructive rather than displacive.

We found that bond switching, which is a prerequisite for the dislocation motion and phase transformation in metals, can also be realized in covalently bonded ceramics through the design of coherent interfaces. However, other factors that contribute to the increased strain and strength of  $\alpha/\beta$ -Si<sub>3</sub>N<sub>4</sub> cannot be excluded, requiring even better illumination of the interactions between the  $\beta \rightarrow \alpha$  phase transformation and stress-strain behaviors. The absolute values of the strain and strength from the compression of nanopillar samples usually differ from those of bulk samples, requiring better fabrication methods to obtain bulk-scale deformable Si<sub>3</sub>N<sub>4</sub> ceramics with dual-phase grand structure and coherent interfaces.

Polymorphism has also been found in other covalent ceramics, which makes it possible to tailor the dual-phase structure with coherent interfaces, especially in those with correlated crystalline structures and atomic distances (e.g., the cubic and hexagonal phases of silicon carbide). In this sense, we anticipate that the approach of our present work can be extended to develop more deformable ceramics.

## REFERENCES AND NOTES

- W. D. Kingery, H. K. Bowen, D. R. Uhlmann, *Introduction to Ceramics* (Wiley, ed. 2, 1976).
- R. N. Katz, *Science* **208**, 841–847 (1980).
- R. Riedel et al., *Nature* **382**, 796–798 (1996).
- T. Ohji, M. Singh, Eds., *Engineered Ceramics: Current Status and Future Prospects* (Wiley, 2016).
- B. R. Golla, A. Mukhopadhyay, B. Basu, S. K. Thimmappa, *Prog. Mater. Sci.* **111**, 100651 (2020).
- P. Baldus, M. Jansen, D. Sporn, *Science* **285**, 699–703 (1999).
- H. A. Bale et al., *Nat. Mater.* **12**, 40–46 (2013).
- N. P. Padture, *Nat. Mater.* **15**, 804–809 (2016).
- B. Lawn, *Fracture of Brittle Solids* (Cambridge Univ. Press, ed. 2, 1993).
- Y.-C. Chen et al., *Phys. Rev. Lett.* **99**, 155506 (2007).
- M. Rühle, A. G. Evans, *Prog. Mater. Sci.* **33**, 85–167 (1989).
- F. Wakai et al., *Nature* **344**, 421–423 (1990).
- P. F. Becher, *J. Am. Ceram. Soc.* **74**, 255–269 (1991).
- B. R. Lawn, N. P. Padture, H. Cai, F. Guiberteau, *Science* **263**, 1114–1116 (1994).
- I. W. Chen, A. Rosenflanz, *Nature* **389**, 701–704 (1997).
- C. A. Wood, H. Zhao, Y. B. Cheng, *J. Am. Ceram. Soc.* **82**, 421–428 (1999).
- Z. Shen, Z. Zhao, H. Peng, M. Nygren, *Nature* **417**, 266–269 (2002).
- W. Clegg, K. Kendall, N. M. N. Alford, T. W. Button, J. D. Birchall, *Nature* **347**, 455–457 (1990).
- M. P. Rao, A. J. Sánchez-Herencia, G. E. Beltz, R. M. McMeeking, F. F. Lange, *Science* **286**, 102–105 (1999).
- E. Munch et al., *Science* **322**, 1516–1520 (2008).
- F. Bouville et al., *Nat. Mater.* **13**, 508–514 (2014).
- K. Zheng et al., *Nat. Commun.* **1**, 24 (2010).
- R. Ramachandramoorthy et al., *Nano Lett.* **19**, 2350–2359 (2019).
- E. J. Frankberg et al., *Science* **366**, 864–869 (2019).
- W. Cai, V. V. Bulatov, J. Chang, J. Li, S. Yip, in vol. 12 of *Dislocations in Solids*, F. R. N. Nabarro, J. P. Hirth, Eds. (Elsevier, 2004), chap. 64.
- J. Li, K. J. Van Vliet, T. Zhu, S. Yip, S. Suresh, *Nature* **418**, 307–310 (2002).
- D. A. Porter, K. E. Easterling, *Phase Transformations in Metals and Alloys* (CRC Press, 2009).
- R. C. Garvie, R. Hannink, R. Pascoe, *Nature* **258**, 703–704 (1975).
- M. Swain, *Nature* **322**, 234–236 (1986).
- R. H. Hannink, P. M. Kelly, B. C. Muddle, *J. Am. Ceram. Soc.* **83**, 461–487 (2000).
- A. Lai, Z. Du, C. L. Gan, C. A. Schuh, *Science* **341**, 1505–1508 (2013).
- A. Liens et al., *Acta Mater.* **183**, 261–273 (2020).
- D. J. Green, R. H. J. Hannink, M. V. Swain, *Transformation Toughening of Ceramics* (CRC Press, 1989).
- J. B. Bilde-Sørensen et al., *Acta Mater.* **44**, 2145–2152 (1996).
- M. W. Lindley, D. J. Godfrey, *Nature* **229**, 192–193 (1971).
- F. L. Riley, *J. Am. Ceram. Soc.* **83**, 245–265 (2000).
- J. Meléndez-Martínez, A. Domínguez-Rodríguez, *Prog. Mater. Sci.* **49**, 19–107 (2004).
- A. Ziegler et al., *Science* **306**, 1768–1770 (2004).
- N. Shibata et al., *Nature* **428**, 730–733 (2004).
- Y. Zhou, H. Hyuga, D. Kusano, Y. Yoshizawa, K. Hirao, *Adv. Mater.* **23**, 4563–4567 (2011).
- D. Hardie, K. Jack, *Nature* **180**, 332–333 (1957).
- C.-M. Wang, X. Pan, M. Rühle, F. L. Riley, M. Mitomo, *J. Mater. Sci.* **31**, 5281–5298 (1996).
- P. Drew, M. Lewis, *J. Mater. Sci.* **9**, 261–269 (1974).
- D. R. Messier, F. Riley, R. Brook, *J. Mater. Sci.* **13**, 1199–1205 (1978).
- Materials and methods are available as supplementary materials.
- T. Csanádi, D. Németh, J. Duszka, Z. Lencsés, P. Šajgalk, *J. Eur. Ceram. Soc.* **36**, 3059–3066 (2016).
- S. Korte, W. Clegg, *Scr. Mater.* **60**, 807–810 (2009).
- Y. Wu et al., *Acta Mater.* **124**, 478–488 (2017).
- A. Zerr et al., *Nature* **400**, 340–342 (1999).
- P. Kroll, *J. Solid State Chem.* **176**, 530–537 (2003).
- B. Xu, J. Dong, P. F. McMillan, O. Shebanova, A. Salamat, *Phys. Rev. B* **84**, 014113 (2011).

## ACKNOWLEDGMENTS

We thank A. Nie (Yanshan University) and Z. Shan, Y. Wang, and W. Xu (Xi'an Jiaotong University) for assistance with the in situ TEM compression characterizations; Z. Quan, Q. Li, and J. Han (Southern University of Science and Technology) for assistance with ADXRD; and Z. Gao (China Academy of Engineering Physics) for providing additional shock experiment support. High-pressure ADXRD experiments were carried out at the beamline 15U1, Shanghai Synchrotron Radiation Facility (SSRF). We also thank L. Zhao (Beihang University) for many discussions and helpful suggestions on both data interpretation and manuscript preparation. **Funding:** This work was supported by the National Key R&D Program of China (no. 2021YFB3702300) and the Strategic Priority Research Program of the Chinese Academy of Sciences (no. XDB30000000). **Author contributions:** K.C. conceived the idea, designed the experiments, and guided the whole project. J.Z., S.M.D., and Y.Y.G. synthesized the samples. J.Z., W.C., F.L., and Z.C. performed the corresponding measurements. S.X.D., Y.Z., and Y.X.G. performed the computational studies. G.L., J.Z., and K.C. wrote the manuscript. All authors contributed to data interpretation and discussed the results. **Competing interests:** The authors declare that they have no competing interests. **Data and materials availability:** All data are available in the manuscript or the supplementary materials. **License information:** Copyright © 2022 the authors, some rights reserved; exclusive licensee American Association for the Advancement of Science. No claim to original US government works. <https://www.science.org/about/science-licenses-journal-article-reuse>

## SUPPLEMENTARY MATERIALS

[science.org/doi/10.1126/science.abq7490](https://doi.org/10.1126/science.abq7490)

Materials and Methods  
Figs. S1 to S22  
Table S1  
References (52–56)  
Movies S1 to S4

Submitted 14 May 2022; accepted 14 September 2022  
10.1126/science.abq7490

## Plastic deformation in silicon nitride ceramics via bond switching at coherent interfaces

Jie ZhangGuanghua LiuWei CuiYiyao GeSongmo DuYixuan GaoYuyang ZhangFei LiZhanglin ChenShixuan DuKexin Chen

*Science*, 378 (6618), • DOI: 10.1126/science.abq7490

### Phasing out fracture

Ceramics are not known for deforming in a plastic manner, instead tending to fracture as a response to loading. J. Zhang *et al.* found a method to avoid fracture and dramatically improve the ductility of silicon nitride (see the Perspective by Frankberg). The authors produced dual-phase silicon nitride samples that turned out to have coherent interfaces between the phases. This configuration allows for two sliding and two-phase transformation steps during loading that circumvent the traditional tendency of bonds to break and materials to fracture. If the mechanism works in other ceramics, then it may be a way to make them more plastic. —BG

### View the article online

<https://www.science.org/doi/10.1126/science.abq7490>

### Permissions

<https://www.science.org/help/reprints-and-permissions>

Use of this article is subject to the [Terms of service](#)

---

*Science* (ISSN ) is published by the American Association for the Advancement of Science. 1200 New York Avenue NW, Washington, DC 20005. The title *Science* is a registered trademark of AAAS.

Copyright © 2022 The Authors, some rights reserved; exclusive licensee American Association for the Advancement of Science. No claim to original U.S. Government Works